CHEMISTRY OF MATERIALS

Article

pubs.acs.org/cm

Tuning Electrical Properties through Control of $TiSe_2$ Thickness in $(BiSe)_{1+\delta}(TiSe_2)_n$ Compounds

Suzannah R. Wood, Devin R. Merrill, Matthias Falmbigl, Daniel B. Moore, Jeffrey Ditto, Marco Esters, and David C. Johnson*

Department of Chemistry, Materials Science Institute, University of Oregon, Eugene, Oregon 97403, United States

Supporting Information

ABSTRACT: A series of $(BiSe)_{1+\delta}(TiSe_2)_n$ compounds where n was varied from two to four were synthesized and electrically characterized to explore the extent of charge transfer from the BiSe layer to the $TiSe_2$ layers. These kinetically stable heterostructures were prepared using the modulated elemental reactants (MER) method, in which thin amorphous elemental layers are deposited in an order that mimics the nanostructure of the desired product. X-ray diffraction (XRD), X-ray area diffraction, and scanning transmission electron microscopy (STEM) data show that the precursors formed the desired products. Specular diffraction scans contain only 00l reflections, indicating that the compounds are crystallographically aligned with the c-axis perpendicular to the substrate. The c-axis lattice parameter increases by 0.604(3) nm with each additional $TiSe_2$ layer. In-plane diffraction scans contain reflections that can be indexed as the (hk0) of the BiSe and $TiSe_2$ constituents. Area diffraction scans are also consistent with the samples containing only BiSe and $TiSe_2$ constituents. Rietveld refinement of the 00l XRD data was used to determine the positions of atomic planes along the c-axis. STEM data supports the structures suggested by the diffraction data and associated refinements but also shows that antiphase boundaries occur approximately 1/3 of the time in the BiSe layers. All samples showed metallic behavior for the temperature-dependent electrical resistivity between 20 K and room temperature. Electrical measurements indicated that charge is transferred from the BiSe layer to the $TiSe_2$ layer. The measured Hall coefficients were all negative indicating that electrons are the majority carrier and are systematically decreased as n was increased. Assuming a single parabolic band model, carrier concentration decreased when the number of $TiSe_2$ layers is increased, suggesting that the amount of charge donated by the BiSe layer to the $TiSe_2$ layers is constant. Seebeck coefficients were negative for all of the $(BiSe)_{1+\delta}(TiSe_2)_n$ compounds studied, indicating that electrons are the majority carrier, and decreased as n increased. The effective mass of the carriers was calculated to be 5−6 m_e for the series of compounds.

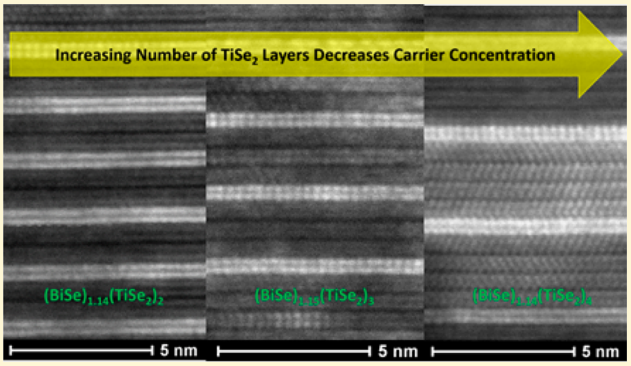

Van der Waals heterostructures consisting of stacks of crystalline two-dimensional (2-D) layers have recently garnered significant interest due to their unusual properties.[1] The vision is that by combining the unique crystal structures and properties of each layer in specific sequences within the heterostructure, "designer devices" with properties and performance that exceed that of the constituents can be achieved.[1] Tunable direct band gap materials have been predicted to result from stacking different metal disulfides and diselenides,[2] and p−n junctions at van der Waals heterostructure interfaces have been experimentally characterized.[3] Charge transfer between constituent layers of heterostructures has been shown to occur at ultrafast time scales.[4] Understanding how to control and modify the interaction between constituents within a heterostructure, including the extent of charge transfer, is essential for achieving the vision of designing optimized nanoscale devices. Systematic changes to a structural unit, a common approach to understand structure−function relationships in synthetic molecular chemistry, will be a valuable tool both to understand and control properties in the emerging field of van der Waals heterostructures.

Ferecrystals are a subset of misfit layered compounds (MLC) with extensive turbostratic disorder between the constituents, which eliminates the structural distortions in the layers caused by the commensurate in-plane axis of MLCs. Ferecrystals are essentially heterostructure analogs of misfit layer compounds. They have the formula $[(MX)_{1+\delta}]_m[TX_2]_n$ (M = Pb, Sn, Bi, Sb, RE; T = transition metal; X = Se or Te). Ferecrystals are synthesized using modulated elemental reactants (MER), a method that uses low temperature annealing of layered precursors consisting of thin layers of the respective elements to access metastable compounds. Because of the short diffusion lengths, a large array of m and n values can be prepared and the

Received: July 6, 2015
Revised: August 19, 2015

DOI: 10.1021/acs.chemmater.5b02572
Chem. Mater. XXXX, XXX, XXX−XXX

sequence of the individual 2D layers can be controlled, resulting in structural isomers.[5] The ability to prepare sequences of compounds with controlled n and m values enables structure−property relationships to be investigated in more detail than previously possible.[6−8] Studies of SnSe-$TiSe_2$ and PbSe-$TiSe_2$ ferecrystals have shown that charge transfer occurs from the MSe layer to the TSe_2 layer.[9−11] $(BiSe)_{1+\delta}(TiSe_2)_1$ showed an increased carrier concentration compared to $(PbSe)_{1+\delta}(TiSe_2)_1$.[11,12]

This work describes the preparation of three new ferecrysals containing a BiSe bilayer: $(BiSe)_{1.14}(TiSe_2)_2$, $(BiSe)_{1.15}(TiSe_2)_3$, and $(BiSe)_{1.14}(TiSe_2)_4$. The c-lattice parameter and distortion of BiSe increases with each additional $TiSe_2$ layer in the heterostructure, with the refined position of atomic planes along the c-axis agreeing with the general structure proposed for the misfit layer compound analogues, $(BiSe)_x(TiSe_2)$ and $(BiSe)_{1.15}(TiSe_2)_2$.[13,14] The differences in electrical resistivity temperature dependences between the crystalline misfit layer compounds and the heterostructure ferecrystals are attributed to different electron−phonon coupling resulting from the turbostratic disorder in the ferecrystals. The systematic change in resistivity in the heterostructures suggests that there is a constant amount of donated charge from the single BiSe layer regardless of the number of $TiSe_2$ layers, and this charge is distributed across the $TiSe_2$ layers. This behavior is similar to that reported for $(BiS)_{1+\delta}(TiS_2)_n$ compounds, where n = 1 and 2.[15,16] In general, the extent of charge transfer between constituents in $(BiX)_{1+\delta}(TX_2)_n$ misfit layer compounds where n = 1, 2 depends on the identity of the transition metal dichalcogenide.[15−17] The single crystal structure of $(BiSe)_{1.08}(TaSe_2)$ was found to have a large in-plane supercell due to antiphase boundaries perpendicular to the a axis, and the antiphase boundaries were used to explain the lack of charge donation from BiSe to $TaSe_2$.[18,19] STEM investigation of the compounds reported herein revealed evidence for similar antiphase boundaries approximately one-third of the time. This may explain the reduced amount of charge transfer observed in this work relative to that previously reported for the $(BiSe)_{1.14}(TiSe_2)_1$ compound.

EXPERIMENTAL SECTION

Precursors designed to form the compounds $(BiSe)_{1+\delta}(TiSe_2)_n$, where $2 \le n \le 4$, were prepared in a custom-built physical vapor deposition system, with pressures below 5×10^{-7} Torr using the modulated elemental reactants (MER) method.[10−12] Elemental bismuth and titanium were deposited with Thermionics electron beam guns, while selenium was deposited with an effusion cell. Quartz crystal microbalances monitored deposition rates, and the elements were deposited with a rate between 0.2 and 0.3 Å/s onto the substrate. Layers of each element were deposited on silicon and fused silica substrates in the order of $(Ti−Se)_p$−Bi−Se, where p equals 2, 3, or 4, repeatedly to give a total film thickness of approximately 50 nm. Samples were annealed between 200 and 400 °C in a nitrogen atmosphere with oxygen below 1.0 ppm for 30 min. Elemental compositions of as deposited and annealed samples were determined via electron probe microanalysis (EPMA) using a Cameca SX 50.[20]

X-ray reflectivity and cross-plane (00l) diffraction were measured on a Bruker D8 Discover (Cu Kα) diffractometer, equipped with a Göbel mirror. These scans were used to measure total film thickness, track as deposited repeat layer thickness, and follow the self-assembly of the precursors. The repeat layer thickness of the as deposited precursors was compared to an estimated c-axis lattice parameter based on the $TiSe_2$ thickness from the reported $[(PbSe)_{1+\delta}]_m(TiSe_2)_n$ ferecrystalline compounds[10,11] and the BiSe thickness based on the reported $[(BiSe)_{1+\delta}]_m(NbSe_2)_n$ compounds.[21] Off-specular, X-ray diffraction scans were acquired on a Rigaku Smartlab (Cu Kα) diffractometer and also on the Multi-Purpose General Scattering beamline 33-BM-C (λ = 1.2653 Å) at the Advanced Photon Source (APS), at Argonne National Laboratory. Rietveld refinements were performed on the cross-plane (00l) scans using the FullProf software suite.[22] In-plane (hk0) diffraction was collected at APS, 33-BM-C, and on a Rigaku Smartlab (Cu Kα) diffractometer for least-squares fits of the lattice parameters (a and b) of the constituents $TiSe_2$ and BiSe, using the WinCSD software package.[23] Area diffraction was collected at APS, 33-BM-C, using a Mar345 image plate detector with θ = 1.0°, 20 s exposure, 180 s acquisition time, and λ = 0.991842 Å.

Scanning transmission electron microscopy (STEM) cross sections were prepared on an FEI Helios 600-Dual Beam focused ion beam (FIB) with a side winder ion column using backside milling methods[24] and wedge premilling methods.[25] High angle annular dark field scanning transmission electron microscopy (HAADF-STEM) was performed on a FEI Titan 80-300 TEM/STEM at 300 keV.

In-plane resistivity and Hall measurements were carried out in the van der Pauw geometry[26] using a custom-built measurement system under vacuum. Samples for these measurements were deposited on fused silica substrates. Electrical contacts were thin copper wires connected to the sample using indium. Samples were measured from 20 to 295 K, and magnetic fields up to 2 T were applied.

RESULTS AND DISCUSSION

In the MER synthetic approach, the design and calibration of the precursor is critical to yield the targeted metastable products. By depositing elemental layers in the order $[Ti−Se]_p$−Bi−Se, where p equals 2, 3, or 4, we control the precursors' layering sequence to mimic the respective target products' final structure, minimizing the diffusion required to form the products. The $TiSe_2$ thickness from the reported $[(PbSe)_{1+\delta}]_n(TiSe_2)_m$ ferecrystalline compounds and the BiSe thickness based on the reported $[(BiSe)_{1+\delta}]_n(NbSe_2)_m$ compounds were used for the initial target repeat layer thickness.[10,11,21] The deposition parameters were scaled so that the repeat layer thickness was close to the targeted repeat layer thickness, and the compositions were adjusted to match the targeted compounds. To evaluate the quality of the precursors, cross-plane XRR and XRD patterns were collected. The as-deposited precursors for the compounds are significantly ordered, exhibiting Bragg diffraction to high angles, suggesting that the compounds begin to self-assemble during the nominally room temperature deposition of the precursors (Figure 1). The optimum annealing conditions were determined by annealing pieces of a precursor designed to form $(BiSe)_{1+\delta}(TiSe_2)_2$ at different temperatures. The resulting diffraction patterns are shown in Figure 1. The positions of the 00l reflections shift to higher 2θ with increasing annealing temperature as the repeating unit decreases in thickness. There is a systematic growth in intensity of the (00l) reflections as temperature is increased. For temperatures below 400 °C, only 00l diffraction maxima are observed, implying the films are highly textured. Above 350 °C, additional peaks appear and can be indexed to textured Bi_2Se_3. The maximum peak intensity, minimum full width at half maxima, and absence of impurity phases (Bi_2Se_3) were observed at 350 °C, which was chosen as the optimal annealing temperature for all samples. This annealing temperature and time are consistent with that reported for $(BiSe)_{1.15}TiSe_2$.[12]

Diffraction patterns from $(BiSe)_{1+\delta}(TiSe_2)_2$, $(BiSe)_{1+\delta}(TiSe_2)_3$, and $(BiSe)_{1+\delta}(TiSe_2)_4$ samples are shown in Figure 2. All the Bragg reflections can be indexed as 00l reflections indicating the films are highly textured. The c-axis lattice parameters calculated from this indexing are contained in

DOI: 10.1021/acs.chemmater.5b02572
Chem. Mater. XXXX, XXX, XXX−XXX

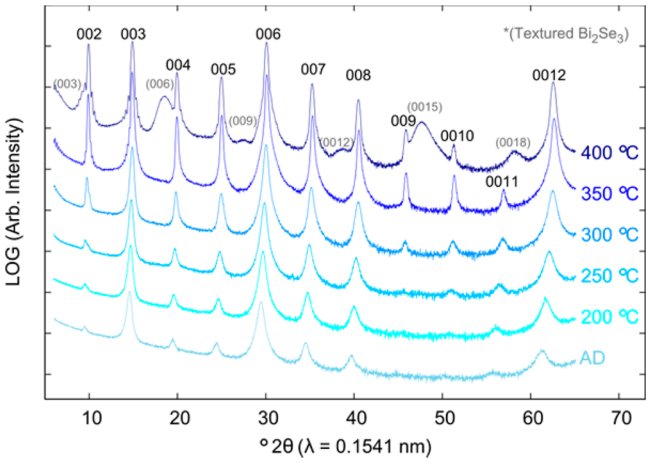

Figure 1. Series of 00l diffraction patterns for a precursor designed to form $(BiSe)_{1+\delta}(TiSe_2)_2$ collected as a function of annealing temperature (offset for clarity). All films were annealed for 30 min at the temperature indicated by the scan, and the scans are offset by arbitrary amounts. The *y*-axis is log intensity to make weak reflections more apparent.

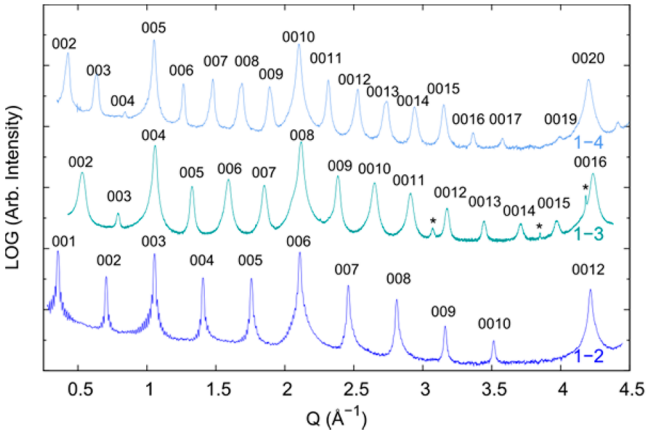

Figure 2. X-ray diffraction patterns of $[(BiSe)_{1+\delta}]_1(TiSe_2)_n$ $(1 - n)$ samples. Compounds are crystallographically aligned with the *c*-axis normal to the substrate so all maxima can be indexed as 00l reflections. Diffraction patterns were collected using two different wavelengths and are shown as log intensity versus *Q* to make weak reflections visible. The scans are offset by arbitrary amounts. The asterisk (*) indicates peaks from the silicon substrate.

Table 1. The *c*-axis lattice parameter systematically increases by 0.603(5) nm with each additional $TiSe_2$ layer. This is larger than the difference between the $(BiSe)_{1.13}(TiSe_2)$ and $(BiSe)_{1.15}(TiSe_2)_2$ MLC's reported by McQueen (0.594 nm).[14] This distance is close to the *c*-axis lattice parameter of 1T-$TiSe_2$ (0.6004 nm),[27] and the difference in *c*-axis lattice parameter between the previously reported $(PbSe)_{1.16}(TiSe_2)$ and $(PbSe)_{1.18}(TiSe_2)_2$ ferecrystals (0.608 nm).[10,11] The BiSe layer thickness obtained by extrapolating to $n = 0$ is 0.58(1) nm. This is similar to the BiSe thickness in ferecrystalline $[(BiSe)_{1.10}]_1(NbSe_2)_m$ compounds (0.59(2) nm)[21] and that reported for $(BiSe)_{1.13}(TiSe_2)$ and $(BiSe)_{1.15}(TiSe_2)_2$ misfit layer compounds (0.593 nm).[14]

Grazing incidence diffraction patterns were collected (Figure 3) to characterize the in-plane structure of the constituents. All

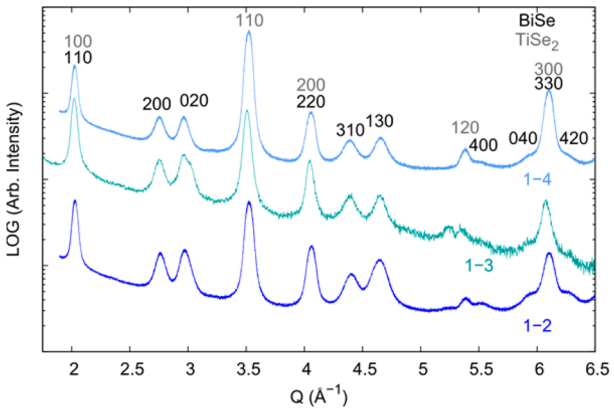

Figure 3. In-plane (*hk*0) diffraction pattern of $[(BiSe)_{1+\delta}]_1(TiSe_2)_n$ $(1 - n)$ samples displaying Bragg peaks and associated indices from the independent lattice structures of both constituents. Diffraction patterns shown in *q*-space because they were collected using two different wavelengths, graphed using log intensity to make weak reflections visible and offset by arbitrary amounts. All films were annealed for 30 min at 350 °C.

peaks can be indexed as (*hk*0) reflections of the two constituents. Only (*hk*0) reflections are observed due to the texture of the samples. For the $(BiSe)_{1+\delta}[TiSe_2]_3$ sample, weak reflections from crystallographically aligned Bi_2Se_3 are also present. The positions of the reflections did not change significantly as the number of $TiSe_2$ layers increased and were consistent with the reflections seen for $(BiSe)_{1.15}TiSe_2$.[12] The relative intensity of the $TiSe_2$ reflections increased as the number of $TiSe_2$ layers in the unit cell was increased and could be indexed using the CdI_2-type structure. The calculated *a*-axis lattice parameters for the $TiSe_2$ constituent of the $n = 2$–4 compounds are contained in Table 1. The lattice parameters of $TiSe_2$ were slightly larger than in the bulk structure (CdI_2-type, $a = 0.3535$ nm)[27] and similar to $TiSe_2$ reported in the ferecrystalline compound $(BiSe)_{1.15}TiSe_2$ ($a = 0.358(6)$ nm),[12] $(PbSe)_{1.16}(TiSe_2)$ ($a = 0.3552(7)$ nm),[11] $(PbSe)_{1.18}(TiSe_2)_2$ ($a = 0.3568(2)$ nm),[10] and $(SnSe)_{1.2}(TiSe_2)$ ($a = 0.37(1)$ nm).[9] The Bragg reflections for BiSe were indexed using the orthorhombic space group *Pcmn*, in contrast to the bulk structure of BiSe, which crystallizes in its own trigonal structure type with an *a*-lattice parameter of 0.415(2) nm.[28] The *a* and *b* lattice parameters (Table 1) compared well with the published $(BiSe)_{1.15}TiSe_2$ ferecrystalline compound ($a = 0.4562(2)$ nm and $b = 0.4242(1)$ nm).[12] The calculated misfit parameters

Table 1. Lattice Parameters and Misfit Parameters for the $(BiSe)_{1+\delta}(TiSe_2)_n$ Compounds Investigated

	repeat thickness	$TiSe_2$ (CdI_2-type)	BiSe (*Pcmn*)	
compound	*c* (nm)	*a* (nm)	*a* (nm)	*b* (nm)
$(BiSe)_{1.14}(TiSe_2)_2$ (1–2)	1.7909 (1)	0.3568(2)	0.4554(1)	0.4235(1)
$(BiSe)_{1.15}(TiSe_2)_3$ (1–3)	2.3741(1)	0.3583(1)	0.4559(4)	0.4243(1)
$(BiSe)_{1.14}(TiSe_2)_4$ (1–4)	2.9941 (1)	0.3565(2)	0.4562(2)	0.4232(1)

DOI: 10.1021/acs.chemmater.5b02572
Chem. Mater. XXXX, XXX, XXX–XXX

were the same as reported for the misfit layer compound $(BiSe)_{1.15}TiSe_2$ and within the expected range for misfit layer compounds (Table 1).[15]

Cross-sectional high angle annular dark field scanning transmission electron microscopy (HAADF-STEM) images were collected to further characterize the structure of these compounds (Figure 4). These images contain the expected layering sequences for $(BiSe)_{1.15}(TiSe_2)_2$, $(BiSe)_{1.14}(TiSe_2)_3$, and $(BiSe)_{1.15}(TiSe_2)_4$ (parts a and b, c, and d of Figure 4, respectively). The images of all three compounds contain brighter BiSe layers and darker $TiSe_2$ layers separated by a van der Waals gap. The BiSe−$TiSe_2$ interface is atomically abrupt in all of the images. The image of $(BiSe)_{1.15}(TiSe_2)_2$ in Figure 4a contains both the substrate and the top carbon coating. The precursor of this sample had 28 $[Ti-Se]_2$−Bi−Se layers as deposited while the image contains ∼26 BiSe−$TiSe_2$−$TiSe_2$ repeats with additional material at the top and bottom of the sample.

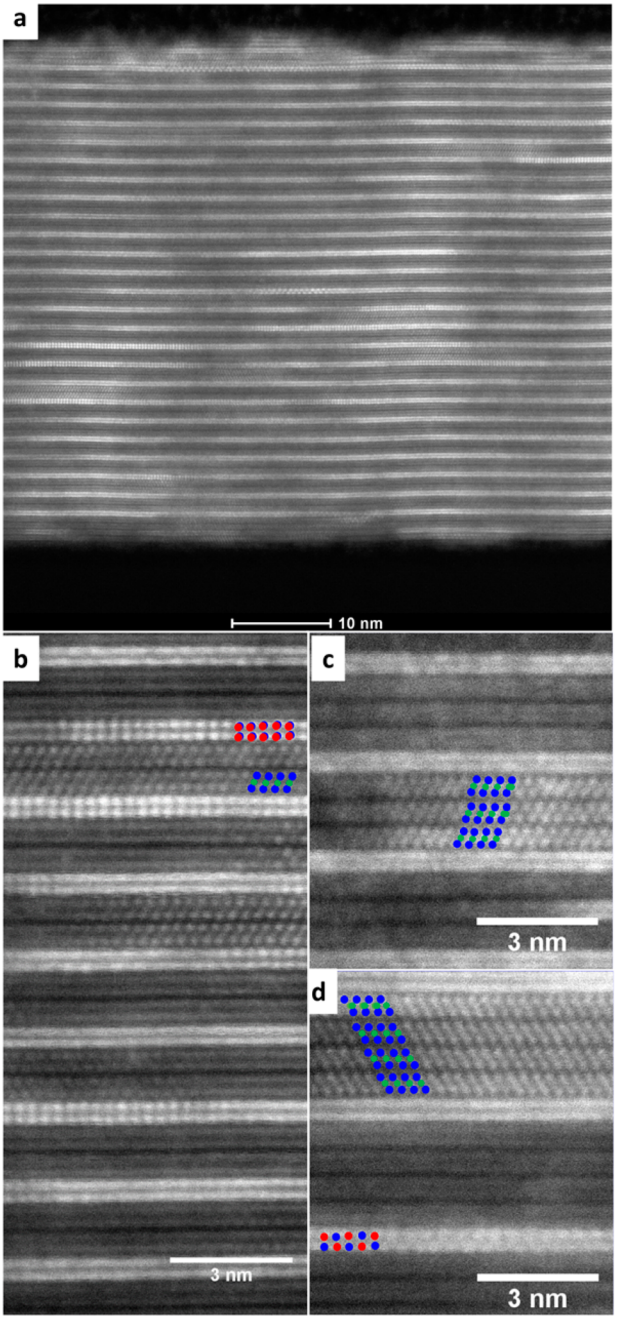

Figure 4. Cross-sectional HAADF-STEM images: (a) a full film cross-section showing alternating BiSe and $TiSe_2$ layers in $(BiSe)_{1.14}(TiSe_2)_2$ and rotational disorder between constituent layers, (b) higher magnification image of a region of the $(BiSe)_{1.14}(TiSe_2)_2$ sample showing the 1-T polymorph of the $TiSe_2$ layer, (c) higher magnification image of a region of the $(BiSe)_{1.15}(TiSe_2)_3$ with a grain boundary in the $TiSe_2$ layer, and (d) a higher magnification image of a region of the $(BiSe)_{1.14}(TiSe_2)_4$ showing the 1T polymorph of the $TiSe_2$ layer and the rotational disorder between constituents.

Different crystal faces of each constituent are present both within a layer and between layers, reflecting the turbostratic disorder of the ferecrystalline structure. The overall stacking sequence is consistent across the samples. The 1T-polytype of $TiSe_2$ can be seen in regions of each of these compounds suggesting an octahedral coordination of the transition metal. While relatively defect free regions were chosen for HAADF-STEM images shown in Figure 4 of the $(BiSe)_{1.15}(TiSe_2)_2$, $(BiSe)_{1.14}(TiSe_2)_3$, and $(BiSe)_{1.15}(TiSe_2)_4$ films, there were regions where defects were observed.

The presence of antiphase boundaries in single crystals of $(BiSe)_{1.10}NbSe_2$ and $(BiSe)_{1.09}TaSe_2$[18,19] lead us to search for these defects in the compounds discussed here. The Bi−Bi bonded pairs resulting from the antiphase boundary are most visible along the (110) zone axis (rock salt setting) of the BiSe. All HAADF-STEM images collected for these samples were examined for this defect in the (110) face. There were a total 25 of (110) faces observed. Of these, 19 were clear enough to distinguish atomic columns. In 7 of these clear images, Bi−Bi pairing was clearly visible (Figure 5). This is the first time this

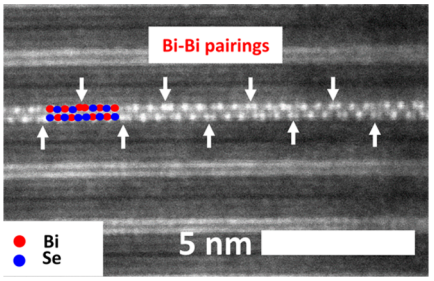

Figure 5. High magnification cross-sectional HAADF-STEM image of $(BiSe)_{1.14}(TiSe_2)_2$ showing the Bi−Bi bonded pairs resulting from the antiphase boundary are most visible along the (110) zone axis (rock salt setting) of the BiSe.

distortion has been seen in $TiSe_2$ containing misfit compounds. As discussed by Wiegers,[15] the antiphase distortion does not alter the position or intensities of the parent face center cubic in-plane cell, so the diffraction data is consistent with the average local structure.

The STEM images were used to create models of the structures of $(BiSe)_{1.14}(TiSe_2)_2$, $(BiSe)_{1.15}(TiSe_2)_3$, and $(BiSe)_{1.14}(TiSe_2)_4$, along the *c* axis, which were then refined using the 00*l* diffraction data to obtain the distance between atomic planes along the *z*-axis (Figure 6; refinements Supporting Information Figures S1−S3, Tables S1−S3). The refinement of $(BiSe)_{1.14}(TiSe_2)_2$ converged to a *c*-lattice parameter of 17.9094(6) Å, which is larger than in the corresponding misfit layer compound (17.8103(1) Å).[14] Within the BiSe layer, the Bi and Se atoms were not in the same plane but were distorted by 19 pm from an ideal 001 plane. This distortion is similar to

DOI: 10.1021/acs.chemmater.5b02572
Chem. Mater. XXXX, XXX, XXX−XXX

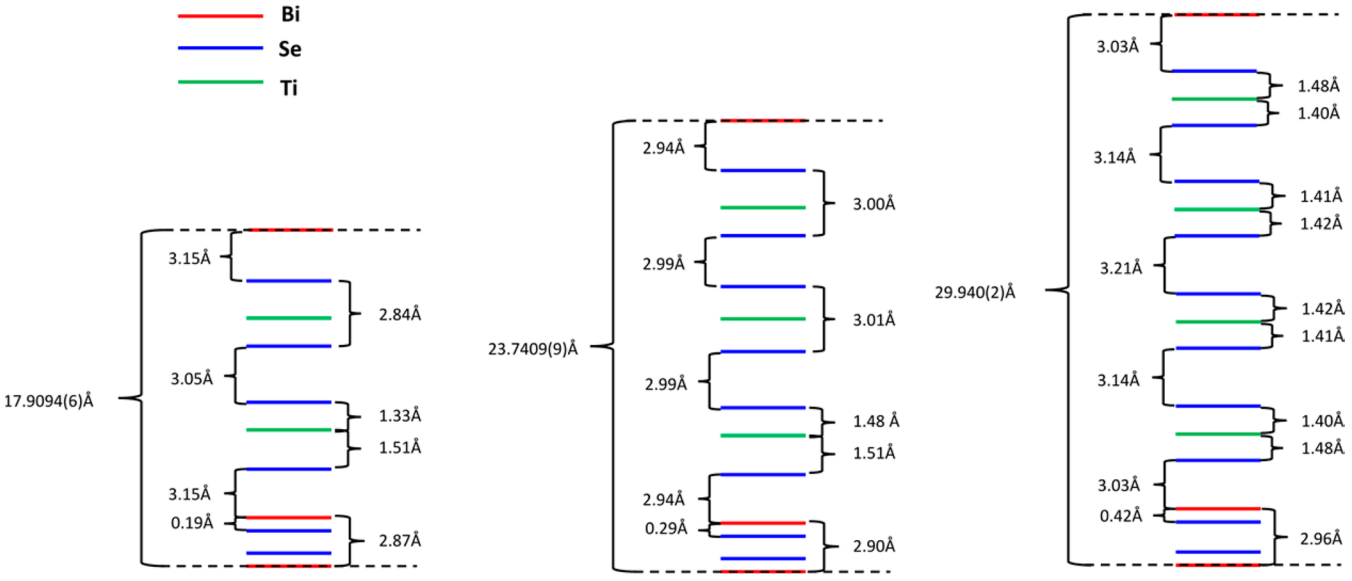

Figure 6. Models for the refined atomic plane positions in $(BiSe)_{1.14}(TiSe_2)_2$, $(BiSe)_{1.15}(TiSe_2)_3$, and $(BiSe)_{1.14}(TiSe_2)_4$. The dashed lines indicate the unit cell. The models for the Rietveld refinement of 00*l* diffraction patterns were based on the constituents BiSe and $TiSe_2$ as determined by *hk*0 diffraction. For each compound Bi is puckered toward the dichalcogenide.

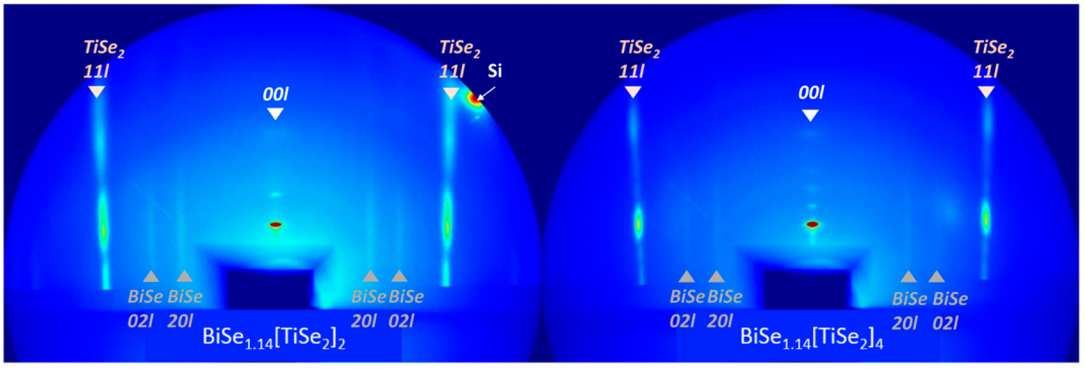

Figure 7. Area X-ray diffraction data for $(BiSe)_{1.14}(TiSe_2)_2$ and $(BiSe)_{1.14}(TiSe_2)_4$ compounds indicate turbostratic disorder.

the distortion in SnSe in the ferecrystal $(SnSe)_{1.2}TiSe_2$ (27 pm).[9] There are two different refined Ti−Se distances (151 and 133 pm); different Ti−Se distances were also reported in the refinement of the atomic planes of $(PbSe)_{1.18}(TiSe_2)_2$.[10] These distances correspond to the distance from Ti to the Se plane bordering the BiSe layer and to the Se plane bordering the second $TiSe_2$ layer, respectively. The refinement of $(BiSe)_{1.14}(TiSe_2)_3$ converged to a *c*-lattice parameter of 23.7409(9) Å. Within the BiSe layer, the Bi and Se atoms are distorted by 29 pm from an ideal 00l plane. While there are two different refined Ti−Se distances, these distances are more similar than the distances in $(BiSe)_{1.14}(TiSe_2)_2$. The 00*l* refinement of $(BiSe)_{1.14}(TiSe_2)_4$ converged to a *c*-lattice parameter of 29.940(2) Å. Within the BiSe layer, the Bi and Se atoms were not in the same plane but were distorted 42 pm from an ideal 001 plane. This suggests an ionic interaction between the Bi cation in the rock salt and the Se anion increases, and the puckering distortion of the BiSe bilayer becomes larger. This increase in puckering leads to a larger distance between Bi atomic planes and a smaller distance between Se atomic planes within a BiSe layer, as the number of $TiSe_2$ layers increases. The Se−Ti distance adjacent to BiSe is larger than the distance adjacent to $TiSe_2$. This also indicates a stronger covalent interaction between the Bi in the rock salt-like layer and the adjacent Se of the $TiSe_2$ layer.

Area diffraction scans were collected to better understand the three-dimensional structure of the films (Figure 7). Sharp reflections are observed along the 00*l* direction due to the regular and coherent spacing of the atomic planes along the *c*-axis. Diffuse scattering occurs along the *l* direction for $h + k \neq 0$. The broadening of these (*hkl*) reflections where $h + k \neq 0$ results from a shortened coherence length in the direction of the reflection, which was reflected in the rotational disorder of the different constituents observed in the STEM images. The sharp (*hk*0) reflections presented earlier in Figure 3 indicate that the individual layers have much larger in-plane coherence lengths. The combination of very broad *hkl* reflection but sharp 00*l* and *hk*0 reflections is consistent with turbostratically disordered layers.[29]

Area diffraction also provided additional insight into the structure of the constituent layers. The broad relatively intense reflections along the $TiSe_2$ (11*l*) direction result from the $TiSe_2$ structure and do not reflect the *c*-axis of the compounds. The increased sharpness of this reflection for $(BiSe)_{1.15}(TiSe_2)_4$ compared to $(BiSe)_{1.15}(TiSe_2)_2$ results from a longer coherence length in this direction, which is consistent with the ordered 1T-polytype structure observed in the HAADF-STEM images

DOI: 10.1021/acs.chemmater.5b02572
Chem. Mater. XXXX, XXX, XXX−XXX

where all layers within one block of $TiSe_2$ exhibit the same crystallographic orientation. The two weak broad maxima at lower angles along the (11*l*) direction result from incomplete destructive interference from the four layers in each block.

The ratio of bismuth to titanium in the compounds was measured using electron probe microanalysis and was also calculated based on the misfit parameter (Table 2). All

Table 2. Bi/Ti Ratio Measured by EPMA and Calculated from Misfit Parameter (δ)

compound	measured Bi/Ti using EPMA	calculated Bi/Ti from fit of *hk*0 diffraction (δ)	calculated Bi/Ti from refinement of 00*l* diffraction (δ)
$(BiSe)_{1.14}(TiSe_2)_2$ (1–2)	0.44(5)	0.57	0.54
$(BiSe)_{1.15}(TiSe_2)_3$ (1–3)	0.33(1)	0.38	0.33
$(BiSe)_{1.14}(TiSe_2)_4$ (1–4)	0.23(1)	0.29	0.29

compounds were found to be bismuth poor in comparison to the expected Bi/Ti ratio based on the misfit parameters. The misfit parameters were determined based on the in-plane lattice parameters of the constituents BiSe and $TiSe_2$ from the *hk*0 diffraction data. The misfit parameter was also determined from the Rietveld refinement of the 00*l* diffraction. While there appears to be a discrepancy in the Bi/Ti ratio, the EPMA measures the average film composition and not necessarily the composition of the refined crystalline component. The presence of defects in the films, the material at the top and the bottom of the film, and the loss of one or more layers relative to the deposited precursor are consistent with the difference between Bi/Ti ratios measured using EPMA and calculated from lattice parameters. While there are defects in the films, the structure found from the refinement of the diffraction data is consistent with the local structure observed via HAADF-STEM within the respective uncertainties.

Electrical Properties. Temperature dependent resistivity data for the series of compounds is compared to the published ferecrystal and misfit layer compound analogues in Figure 8.[12,14] For the compounds reported in this study, the electrical properties were measured from samples synthesized using the same equipment cycle; this minimizes differences in composition and defect density.[30,31] As seen in Figure 8, the temperature dependent resistivities of two different samples

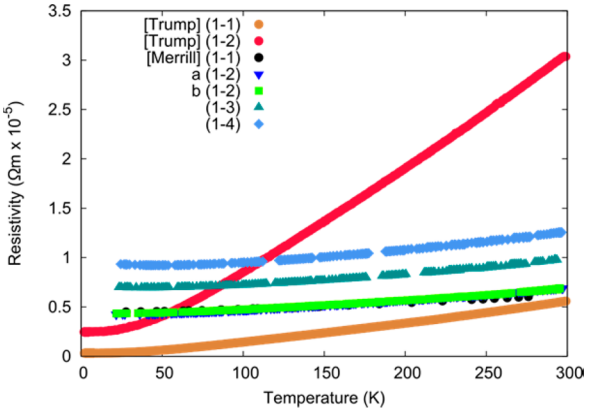

Figure 8. Temperature-dependent resistivity of the $[(BiSe)_{1+\delta}]_1(TiSe_2)_n$ $(1 - n)$ ferecrystalline compounds is compared to the published temperature dependent resistivity for the ferecrystal $(BiSe)_{1.15}TiSe_2$[12] and MLC $(BiSe)_{1.13}TiSe_2$ and $(BiSe)_{1.15}(TiSe_2)_2$.[14]

of the ferecrystalline compound $(BiSe)_{1.14}(TiSe_2)_2$ are the same within experimental error, demonstrating the reproducibility of the electrical measurements within a deposition cycle. The magnitude of resistivity of these compounds is consistent with a low conductivity metal or a semimetal. While both the ferecrystal $(BiSe)_{1.14}(TiSe_2)_2$ and the MLC compound $(BiSe)_{1.15}(TiSe_2)_2$ have the same magnitude of resistivity, the compound synthesized using the MER technique shows a significantly smaller temperature dependence. To understand this difference, the data was fit to the Bloch–Grüneisen equation. The Bloch–Grüneisen equation describes metallic resistivity:

$$\rho(T) = \rho_0 + \Re\left(\frac{T}{\theta_D}\right)^5 \int_0^{\theta_D/T} \frac{z^5}{(e^z - 1)(1 - e^{-z})}\,dz \quad (1)$$

where ρ_0 is the residual resistivity, $\Re$ is the electron–phonon interaction constant, and θ_D is the Debye temperature.[32] Fits to the Bloch–Grüneisen equation revealed a 6–7 times stronger electron–phonon interaction in the MLC compound, $(BiSe)_{1.15}(TiSe_2)_2$, compared to the analogous ferecrystalline compound, $(BiSe)_{1.14}(TiSe_2)_2$, a consequence of the rotational disorder in the ferecrystalline polymorph (Supporting Information, Figure S4). A similar difference between the electron–phonon interaction in misfit layer compounds and ferecrystalline compounds was observed in $(PbSe)_{1.16}(TiSe_2)_2$ and $(PbSe)_{1.18}(TiSe_2)_2$.[10] While the Bloch–Grüneisen equation provides valuable insight into the difference in electron–phonon interactions, this equation does not account for the slight upturn in the resistivity data at low temperatures. While this upturn is less prominent than in the $(PbSe)_{1.18}(TiSe_2)_2$ and $(SnSe)_{1.2}(TiSe_2)$ ferecrystal analogues,[9,10] it indicates that electron–electron correlations and localization of carriers occurs in these BiSe-$TiSe_2$ containing polymorphs.[33]

The systematic increase in the resistivity and the similarity of temperature dependence as the number of $TiSe_2$ layers increases from 2 to 4 for the ferecrystals reported here invites comparison to bulk 1T-$TiSe_2$, the eventual end member of this series where $n = \infty$. At room temperature, pristine, bulk 1T-$TiSe_2$ has a reported resistivity between 1×10^{-5} Ω m and 15.6×10^{-5} Ω m.[14,34,35] The room temperature resistivity values of the ferecrystals reported here reasonably converge to the reported room temperature resistivity. However, the temperature dependence of these compounds differs significantly from bulk 1T-$TiSe_2$, which exhibits a broad feature below 200 K attributed to the onset of a charge density wave (CDW).[14,34–38] There is no analogous feature in the temperature-dependent resistivity of the reported compounds that suggests the presence of a CDW. This is consistent with prior reports of $TiSe_2$ containing crystalline MLCs[14,16,39] and the ferecrystalline analogues.[9–12] Historically, the absence of CDW in MLCs has been explained by the structural distortion of the TX_2 layer due to long-range periodic interaction between the constituents.[15] To our knowledge, the only misfit layer compounds to exhibit a charge density wave are tin vanadium selenide ferecrystals, due to turbostratic disorder and low dimensionality of the dichalogenide.[40–43] In bulk 1T–$TiSe_2$, the CDW is formed by electron–phonon coupling and can be suppressed by increases in the carrier concentration.[38,44]

To investigate the absence of the CDW and whether the increase in resistivity with increased $TiSe_2$ layers is due to a change in carrier concentration or carrier mobility, temper-

DOI: 10.1021/acs.chemmater.5b02572
Chem. Mater. XXXX, XXX, XXX–XXX

ature-dependent Hall coefficients were measured and compared to the previously published ferecrystal $(BiSe)_{1.15}(TiSe_2)$ (Figure 9a).[12] The Hall coefficients for the samples are negative, indicating that electrons are the majority carrier type. Electrons were also found to be the carriers in the ferecrystal analogues $(SnSe)_{1.2}(TiSe_2)$[9] and $(PbSe)_{1.18}(TiSe_2)_2$[10] and for the analogue $(MS)_{1+x}(TiS_2)_2$ (M = Pb, Bi, Sn) misfit layer compounds.[16] For the $(BiSe)_{1+\delta}(TiSe_2)_n$ compounds, there is a systematic increase in magnitude of the Hall coefficient as the number of layers of $TiSe_2$ increases. Assuming a single band model, the Hall coefficient is inversely proportional to the carrier concentration, and carrier concentrations calculated using a single band model are compared to the previously published ferecrystal $(BiSe)_{1.15}(TiSe_2)$ in Figure 9b.[12] The carrier concentration decreases as the temperature decreases for all samples and decreases with each additional layer of $TiSe_2$. The carrier concentration agrees well with the high temperature carrier concentration reported by Wan for the misfit layer compound $(BiS)_{1.2}(TiS_2)_2$.[16] The carrier concentration for all the reported ferecrystals was found to be an order of magnitude higher than bulk selenium-deficient $TiSe_{2-x}$;[38] This may explain the absence of CDWs in these materials, despite similar room temperature resistivity values. Temperature dependent mobility determined from resistivity measurements and from Hall measurements are compared to the previously published ferecrystal $(BiSe)_{1.15}(TiSe_2)$ in Figure 9c.[12] The mobility of carriers increases as the temperature decreases for all compounds. The similarity of mobility suggests that the $TiSe_2$ is the conducting layer in all of these compounds. Similar values for the mobility of the compounds prepared here would not be expected assuming a rigid band model since the carrier concentration changes. A rigid band model is an over-simplification, however, as the structure of the constituents change as n is increased. The mobility of the published ferecrystal $(BiSe)_{1.15}(TiSe_2)$ is lower than the ferecrystalline compounds investigated here. This is likely due to a slight difference in composition and defect density.[30,31] Neglecting the previously published $(BiSe)_{1.15}(TiSe_2)$, the difference in temperature dependent resistivity is due to differences in the carrier concentration.

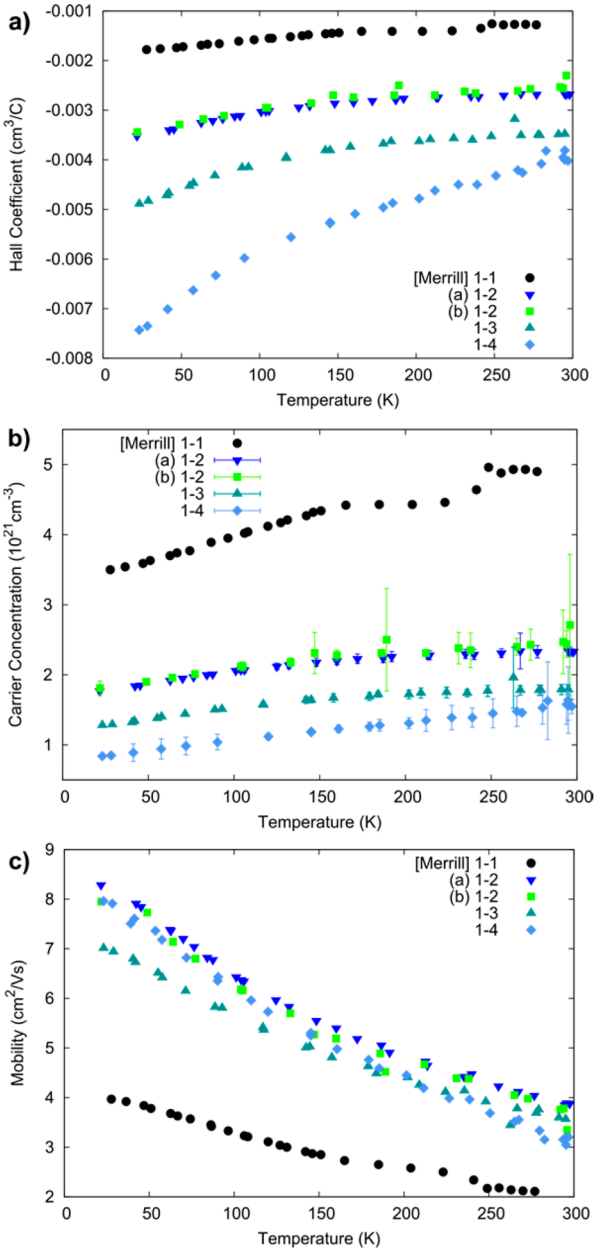

Figure 9. Temperature-dependent (a) Hall coefficients, (b) carrier concentrations, and (c) mobilities. (a) Temperature-dependent Hall coefficients for the ferecrystalline compounds $[(BiSe)_{1+\delta}]_1(TiSe_2)_n$ (1 − n) are compared to the previously published ferecrystal $(BiSe)_{1.15}TiSe_2$.[12] (b) Temperature-dependent carrier concentration calculated using a single band model for the ferecrystalline compounds $[(BiSe)_{1+\delta}]_1(TiSe_2)_n$ (1 − n) including previously published $(BiSe)_{1.15}TiSe_2$.[12] (c) Temperature-dependent mobilities calculated using a single band model for the ferecrystals including previously published $(BiSe)_{1.15}TiSe_2$.[12]

Previous work with $(BiX)_{1+\delta}(TX_2)_n$ misfit layer compounds indicates that the amount of charge transfer between (BiX) and the (TX_2) constituents depends on the transition metal in the dichalcogenide, and that the antiphase distortion in BiX also depends on the amount of charge transfer. A lack of electron donation from BiX layers to the NbX_2 layer is reported, while electron donation is suggested to occur from the BiS layers to the CrS_2 layers[15] and from the BiSe layers to $CrSe_2$ layers.[17] As seen in Figure 9b, the carrier concentration decreases with each additional layer of $TiSe_2$ suggesting that BiSe acts as an electron donor and $TiSe_2$ acts as an electron acceptor, as previously suggested in literature for BiX-TiX_2 containing intergrowths.[9,15,16] In the misfit layer compound $(BiS)_{1.2}(TiS_2)_2$, 0.45 carriers (electrons) per Ti atom are received from the BiS layer.[16] To investigate how charge is transferred between constituent layers, the carrier concentration was normalized to the number of Bi atoms per unit volume and to the number of Ti atoms per unit volume (Figures 10a,b, respectively). While there is a systematic trend for the overall carrier concentration, this trend does not persist when the carrier concentration is normalized to the number of Bi atoms. Instead the carriers donated per Bi atom is approximately the same for the ferecrystal compounds $(BiSe)_{1.14}(TiSe_2)_2$, $(BiSe)_{1.15}(TiSe_2)_3$, and $(BiSe)_{1.14}(TiSe_2)_4$. For all compounds the number of carriers per Bi atom decreases as the temperature decreases.

A systematic trend in the total carrier concentration is also observed when the carrier concentration is normalized to the number of Ti atoms per unit volume. The number of carriers systematically decreases as the number of $TiSe_2$ layers increases. If a constant number of carriers is transferred from the BiSe layer into the $TiSe_2$ layers and just distributed over an

DOI: 10.1021/acs.chemmater.5b02572
Chem. Mater. XXXX, XXX, XXX−XXX

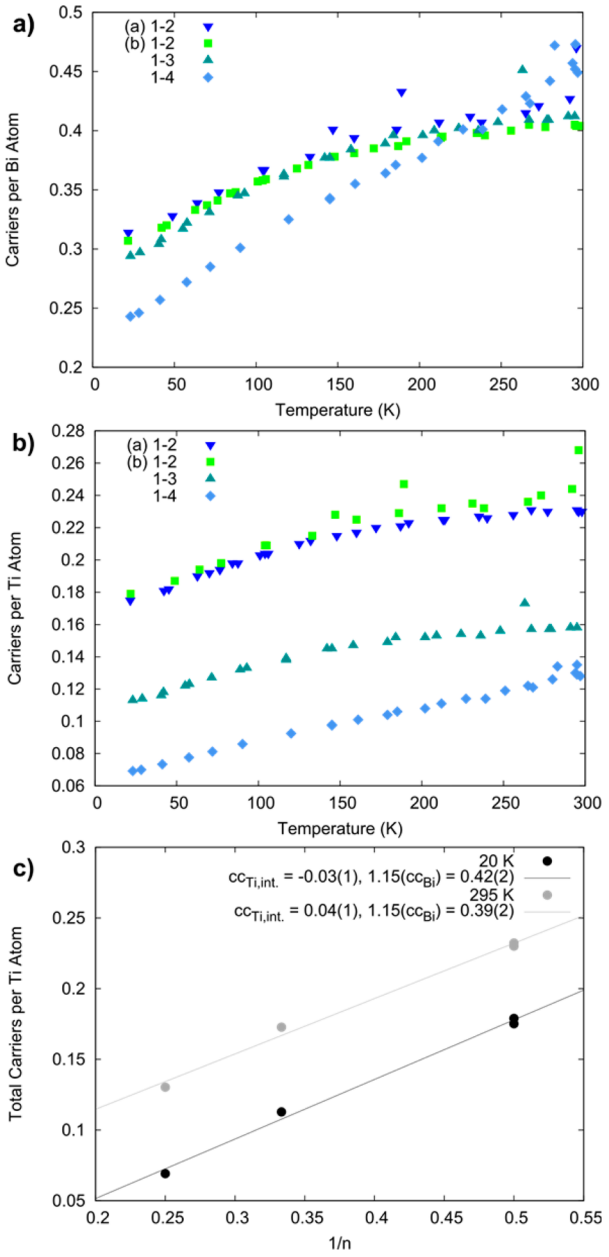

Figure 10. Temperature-dependent carrier concentrations (a) normalized to the number of Bi atoms per unit volume and (b) normalized to the number of Ti atoms per unit volume for the ferecrystalline compounds $[(BiSe)_{1+\delta}]_1(TiSe_2)_n$ $n = 2-4$ and (c) total carriers per Ti atom at 20 and 295 K vs $1/n$ for ferecrystalline compounds $[(BiSe)_{1+\delta}]_1(TiSe_2)_n$ for $n = 2-4$.

increasing number of $TiSe_2$ layers (n), then the following equation should hold:

$$cc_{Ti,tot} = cc_{Ti,i} + \frac{1.15cc_{Bi}}{n} \quad (2)$$

where $cc_{Ti,tot}$ is the total number of carrier per Ti atom, $cc_{Ti,i}$ the number of intrinsic $TiSe_2$ carriers per $TiSe_2$ atom, and cc_{Bi} is the amount of donated carriers from the BiSe layer per Ti atom (Figure 10c). As seen in Figure 10c, this simple model appears to apply for the ferecrystalline compounds $(BiSe)_{1.14}(TiSe_2)_2$, $(BiSe)_{1.15}(TiSe_2)_3$, and $(BiSe)_{1.14}(TiSe_2)_4$. At both room temperature and 20 K approximately 0.35 carriers per Bi atom are donated into the conduction band of $TiSe_2$.

To further characterize the carriers in the material, room temperature Seebeck coefficients of the ferecrystalline compounds $(BiSe)_{1+\delta}(TiSe_2)_n$ were measured (Table 3). The

Table 3. Seebeck Coefficients of $(BiSe)_{1+\delta}(TiSe_2)_n$ at Room Temperature

compound	Seebeck coefficient (μV/K)
$(BiSe)_{1.14}(TiSe_2)_2$ (1−2)	−65
$(BiSe)_{1.15}(TiSe_2)_3$ (1−3)	−68
$(BiSe)_{1.14}(TiSe_2)_4$ (1−4)	−80

negative sign of the Seebeck coefficients indicates that electrons are the charge carriers in the ferecrystalline compounds, which is consistent with the sign of the Hall coefficients (Figure 9a). The magnitude of the Seebeck coefficient increases with the number of $TiSe_2$ layers, which is consistent with the decrease in carrier concentration. For metals, under a single parabolic band and assuming energy independent scattering, the Seebeck coefficient is given by

$$\alpha = \frac{8\pi^2 k_B^2}{3eh^2} m^* T \left(\frac{\pi}{3n}\right)^{2/3} \quad (3)$$

where n is the carrier concentration and m^* is the effective mass of the carrier.[45] Equation 3 was used to calculate the effective mass of the electron for each ferecrystalline compound $(BiSe)_{1+\delta}(TiSe_2)_n$ ($n = 2-4$) yielding a value of 5−6 m_e. This compares well with the effective carrier mass for the MLC $(BiS)_{1.2}(TiS_2)_2$ (6.3 m_e).[16]

CONCLUSIONS

The synthesis, structure, and electrical properties of three new heterostructures, $(BiSe)_{1.14}(TiSe_2)_2$, $(BiSe)_{1.15}(TiSe_2)_3$, and $(BiSe)_{1.14}(TiSe_2)_4$, consisting of a bilayer of BiSe and the trilayer $TiSe_2$ dichalogenide were discussed. The compounds were formed from designed precursors. With each additional $TiSe_2$ layer, the c-axis lattice parameter increased by 0.603(5) nm. The structure of the compounds suggests charge transfer occurs, which is confirmed by electrical transport measurements. All samples displayed a lower temperature dependence in the resistivity data than MLC compounds due to decreased electron−phonon coupling. As the number of $TiSe_2$ layers is increased, the number of carriers are decreased while maintaining the same carrier mobility and effective carrier mass. This suggests it might be possible to tune electrical properties by modulating the nanostructure of the heterostructures by controlling the charge transfer between constituents.

ASSOCIATED CONTENT

Supporting Information

The Supporting Information is available free of charge on the ACS Publications website at DOI: 10.1021/acs.chemmater.5b02572.

Rietveld refinement analysis with fit parameters and Bloch-Grüeneisen fits with fit parameters (PDF)

AUTHOR INFORMATION

Corresponding Author

*(D.C.J.) E-mail: davej@uoregon.edu.

Notes

The authors declare no competing financial interest.

DOI: 10.1021/acs.chemmater.5b02572
Chem. Mater. XXXX, XXX, XXX−XXX

■ ACKNOWLEDGMENTS

The authors acknowledge support from the National Science Foundation under Grant DMR-1266217. Coauthors M.F., S.R.W., and M.E. acknowledge support from the National Science Foundation through CCI Grant Number CHE-1102637. The authors thank Evguenia A. Karapetrova at 33-BM-C for technical assistance during collection of the synchrotron XRD data. Use of the Advanced Photon Source was supported by the U.S. Department of Energy, Office of Science, Office of Basic Energy Sciences, under Contract No. DE-AC02-06CH11357.

■ REFERENCES

(1) Geim, A. K.; Grigorieva, I. V. Van Der Waals Heterostructures. *Nature* **2013**, *499*, 419−425.

(2) Terrones, H.; López-Urías, F.; Terrones, M. Novel Hetero-Layered Materials with Tunable Direct Band Gaps by Sandwiching Different Metal Disulfides and Diselenides. *Sci. Rep.* **2013**, *3*, 1549.

(3) Lee, C.-H.; Lee, G.-H.; van der Zande, A. M.; Chen, W.; Li, Y.; Han, M.; Cui, X.; Arefe, G.; Nuckolls, C.; Heinz, T. F.; et al. Atomically Thin P−N Junctions with van der Waals Heterointerfaces. *Nat. Nanotechnol.* **2014**, *9*, 676−681.

(4) Hong, X.; Kim, J.; Shi, S.-F.; Zhang, Y. Y.; Jin, C.; Sun, Y.; Tongay, S.; Wu, J.; Zhang, Y. Y.; Wang, F. Ultrafast Charge Transfer in Atomically Thin MoS_2/WS_2 Heterostructures. *Nat. Nanotechnol.* **2014**, *9*, 682−686.

(5) Esters, M.; Alemayehu, M. B.; Jones, Z.; Nguyen, N. T.; Anderson, M. D.; Grosse, C.; Fischer, S. F.; Johnson, D. C. Synthesis of Inorganic Structural Isomers By Diffusion-Constrained Self-Assembly of Designed Precursors: A Novel Type of Isomerism. *Angew. Chem., Int. Ed.* **2015**, *54*, 1130−1134.

(6) Alemayehu, M. B.; Mitchson, G.; Ditto, J.; Hanken, B. E.; Asta, M.; Johnson, D. C. Charge Transfer between PbSe and $NbSe_2$ in $[(PbSe)_{1.14}]_m(NbSe_2)_1$ Ferecrystalline Compounds. *Chem. Mater.* **2014**, *26*, 1859−1866.

(7) Alemayehu, M. B.; Falmbigl, M.; Ta, K.; Grosse, C.; Westover, R. D.; Bauers, S. R.; Fischer, S. F.; Johnson, D. C. Structural and Electrical Properties of $([SnSe]_{1+\delta})_m(NbSe_2)_1$ Compounds: Single $NbSe_2$ Layers Separated by Increasing Thickness of SnSe. *Chem. Mater.* **2015**, *27*, 867−875.

(8) Alemayehu, M. B.; Ta, K.; Falmbigl, M.; Johnson, D. C. Charge Transfer vs. Dimensionality: What Affects the Transport Properties of Ferecrystals? *Nanoscale* **2015**, *7*, 7378−7385.

(9) Merrill, D. R.; Moore, D. B.; Ditto, J.; Sutherland, D. R.; Falmbigl, M.; Winkler, M.; Pernau, H.-F.; Johnson, D. C. The Synthesis, Structure, and Electrical Characterization of $(SnSe)_{1.2}TiSe_2$. *Eur. J. Inorg. Chem.* **2015**, *2015*, 83−91.

(10) Moore, D. B.; Beekman, M.; Disch, S.; Zschack, P.; Häusler, I.; Neumann, W.; Johnson, D. C. Synthesis, Structure, and Properties of Turbostratically Disordered $(PbSe)_{1.18}(TiSe_2)_2$. *Chem. Mater.* **2013**, *25*, 2404−2409.

(11) Moore, D. B.; Stolt, M. J.; Atkins, R.; Sitts, L.; Jones, Z.; Disch, S.; Beekman, M.; Johnson, D. C. Structural and Electrical Properties of $(PbSe)_{1.16}TiSe_2$. *Emerging Mater. Res.* **2012**, *1*, 292−298.

(12) Merrill, D. R.; Moore, D. B.; Coffey, M. N.; Jansons, A. W.; Falmbigl, M.; Johnson, D. C. Synthesis and Characterization of Turbostratically Disordered $(BiSe)_{1.15}TiSe_2$. *Semicond. Sci. Technol.* **2014**, *29*, 064004.

(13) Oosawa, Y.; Gotoh, Y.; Akimoto, J.; Onoda, M. Preparation and Characterization of Bi-Containing Ternary Chalcogenides with Layered Composite Crystal Structure. *J. Alloys Compd.* **1991**, *176*, 319−327.

(14) Trump, B. A.; Livi, K. J. T.; McQueen, T. M. The New Misfit Compound $(BiSe)_{1.15}(TiSe_2)_2$ and the Role of Dimensionality in the $Cu_x(BiSe)_{1+\delta}(TiSe_2)_n$ Series. *J. Solid State Chem.* **2014**, *209*, 6−12.

(15) Wiegers, G. A. Misfit Layer Compounds: Structures and Physical Properties. *Prog. Solid State Chem.* **1996**, *24*, 1−139.

(16) Wan, C.; Wang, Y.; Wang, N.; Koumoto, K. Low-Thermal-Conductivity $(MS)_{1+x}(TiS_2)_2$ (M = Pb, Bi, Sn) Misfit Layer Compounds for Bulk Thermoelectric Materials. *Materials* **2010**, *3*, 2606−2617.

(17) Clarke, S. M.; Freedman, D. E. $(BiSe)_{1.23}CrSe_2$ and $(BiSe)_{1.22}(Cr_{1.2}Se_2)_2$: Magnetic Anisotropy in the First Structurally Characterized Bi-Se-Cr Ternary Compounds. *Inorg. Chem.* **2015**, *54*, 2765−2771.

(18) Zhou, W. Y.; Meetsma, A.; de Boer, J. L.; Wiegers, G. A. Characterization and Electrical Transport Properties of the Misfit Layer Compounds $(BiSe)_{1.10}NbSe_2$ and $(BiSe)_{1.09}TaSe_2$. *Mater. Res. Bull.* **1992**, *27*, 563−572.

(19) Petříček, V.; Cisarova, I.; de Boer, J. L.; Zhou, W.; Meetsma, A.; Wiegers, G. A.; van Smaalen, S. The Modulated Structure of the Commensurate Misfit-Layer Compound $(BiSe)_{1.09}TaSe_2$. *Acta Crystallogr., Sect. B: Struct. Sci.* **1993**, *49*, 258−266.

(20) Phung, T. M.; Jensen, J. M.; Johnson, D. C.; Donovan, J. J.; McBurnett, B. G. Determination of the Composition of Ultra-Thin Ni-Si Films on Si: Constrained Modeling of Electron Probe Microanalysis and X-Ray Reflectivity Data. *X-Ray Spectrom.* **2008**, *37*, 608−614.

(21) Heideman, C.; Nyugen, N.; Hanni, J.; Lin, Q.; Duncombe, S.; Johnson, D. C.; Zschack, P. The Synthesis and Characterization of New $[(BiSe)_{1.10}]_m[NbSe_2]_n$, $[(PbSe)_{1.10}]_m[NbSe_2]_n$, $[(CeSe)_{1.14}]_m[NbSe_2]_n$ and $[(PbSe)_{1.12}]_m[TaSe_2]_n$ Misfit Layered Compounds. *J. Solid State Chem.* **2008**, *181*, 1701−1706.

(22) Roisnel, T.; Rodríquez-Carvajal, J. WinPLOTR: A Windows Tool for Powder Diffraction Pattern Analysis. *Mater. Sci. Forum* **2001**, *378*−*381*, 118−123.

(23) Akselrud, L.; Grin, Y. WinCSD: Software Package for Crystallographic Calculations (Version 4). *J. Appl. Crystallogr.* **2014**, *47*, 803−805.

(24) Kang, H.-J.; Kim, J.; Oh, J.; Back, T.; Kim, H. Ultra-Thin TEM Sample Preparation with Advanced Backside FIB Milling Method. *Microsc. Microanal.* **2010**, *16*, 170−171.

(25) Schaffer, M.; Schaffer, B.; Ramasse, Q. Sample Preparation for Atomic-Resolution STEM at Low Voltages by FIB. *Ultramicroscopy* **2012**, *114*, 62−71.

(26) van der Pauw, L. J. A Method of Measuring Specific Resistivity and Hall Effect of Discs of Arbitrary Shape. *Philips Res. Reports* **1958**, *13*, 1−9.

(27) McTaggart, F.; Wadsley, A. The Sulphides, Selenides, and Tellurides of Titanium, Zirconium, Hafnium, and Thorium. I. Preparation and Characterization. *Aust. J. Chem.* **1958**, *11*, 445.

(28) Gobrecht, H.; Boeters, K.-E.; Pantzer, G. Über Kristallstruktur und elektrische Eigenschaften der Wismutselenide Bi_2Se_2 und Bi_2Se_3. *Eur. Phys. J. A* **1964**, *177*, 68−83.

(29) Warren, B. E. X-Ray Diffraction in Random Layer Lattices. *Phys. Rev.* **1941**, *59*, 693−698.

(30) Bauers, S. R.; Moore, D. B.; Ditto, J.; Johnson, D. C. Phase Width of Kinetically Stable $([PbSe]_{1+\delta})_1(TiSe_2)_1$ Ferecrystals and the Effect of Precursor Composition on Electrical Properties. *J. Alloys Compd.* **2015**, *645*, 118−124.

(31) Merrill, D.; Moore, D.; Bauers, S.; Falmbigl, M.; Johnson, D. Misfit Layer Compounds and Ferecrystals: Model Systems for Thermoelectric Nanocomposites. *Materials* **2015**, *8*, 2000−2029.

(32) Ziman, J. M. *Electrons and Phonons: The Theory of Transport Phenomena in Solids*, 1st ed.; Clarendon Press: Oxford, 1960.

(33) Altshuler, B. L.; Khmel'nitzkii, D.; Larkin, A. I.; Lee, P. A. Magnetoresistance and Hall Effect in a Disordered Two-Dimensional Electron Gas. *Phys. Rev. B: Condens. Matter Mater. Phys.* **1980**, *22*, 5142−5153.

(34) Di Salvo, F. J.; Moncton, D. E.; Waszczak, J. V. Electronic Properties and Superlattice Formation in the Semimetal $TiSe_2$. *Phys. Rev. B* **1976**, *14*, 4321−4328.

(35) Kusmartseva, A. F.; Sipos, B.; Berger, H.; Forró, L.; Tutiš, E. Pressure Induced Superconductivity in Pristine 1T−$TiSe_2$. *Phys. Rev. Lett.* **2009**, *103*, 236401.

DOI: 10.1021/acs.chemmater.5b02572
Chem. Mater. XXXX, XXX, XXX−XXX

(36) Woo, K. C.; Brown, F. C.; McMillan, W. L.; Miller, R. J.; Schaffman, M. J.; Sears, M. P. Superlattice Formation in Titanium Diselenide. *Phys. Rev. B* **1976**, *14*, 3242−3247.
(37) Li, G.; Hu, W. Z.; Qian, D.; Hsieh, D.; Hasan, M. Z.; Morosan, E.; Cava, R. J.; Wang, N. L. Semimetal-to-Semimetal Charge Density Wave Transition in 1T-$TiSe_2$. *Phys. Rev. Lett.* **2007**, *99*, 027404.
(38) Bhatt, R.; Bhattacharya, S.; Basu, R.; Ahmad, S.; Chauhan, a. K.; Okram, G. S.; Bhatt, P.; Roy, M.; Navaneethan, M.; Hayakawa, Y.; et al. Enhanced Thermoelectric Properties of Selenium-Deficient Layered $TiSe_{2-x}$: A Charge-Density-Wave Material. *ACS Appl. Mater. Interfaces* **2014**, *6*, 18619−18625.
(39) Giang, N.; Xu, Q.; Hor, Y. S.; Williams, A. J.; Dutton, S. E.; Zandbergen, H. W.; Cava, R. J. Superconductivity at 2.3 K in the Misfit Compound $(PbSe)_{1.16}(TiSe_2)_2$. *Phys. Rev. B: Condens. Matter Mater. Phys.* **2010**, *82*, 024503.
(40) Atkins, R.; Disch, S.; Jones, Z.; Haeusler, I.; Grosse, C.; Fischer, S. F.; Neumann, W.; Zschack, P.; Johnson, D. C. Synthesis, Structure and Electrical Properties of a New Tin Vanadium Selenide. *J. Solid State Chem.* **2013**, *202*, 128−133.
(41) Atkins, R.; Dolgos, M.; Fiedler, A.; Grosse, C.; Fischer, S. F.; Rudin, S. P.; Johnson, D. C. Synthesis and Systematic Trends in Structure and Electrical Properties of $[(SnSe)_{1.15}]_m(VSe_2)_1$, m = 1, 2, 3, and 4. *Chem. Mater.* **2014**, *26*, 2862−2872.
(42) Falmbigl, M.; Fiedler, A.; Atkins, R. E.; Fischer, S. F.; Johnson, D. C. Suppressing a Charge Density Wave by Changing Dimensionality in the Ferecrystalline Compounds $([SnSe]_{1.15})_1(VSe_2)_n$ with n = 1, 2, 3, 4. *Nano Lett.* **2015**, *15*, 943−948.
(43) Falmbigl, M.; Putzky, D.; Ditto, J.; Esters, M.; Bauers, S. R.; Ronning, F.; Johnson, D. C. Influence of Defects on the Charge Density Wave of $([SnSe]_{1+\delta})_1(VSe_2)_1$ Ferecrystals. *ACS Nano* **2015**, DOI: 10.1021/acsnano.5b03361.
(44) Bhatt, R.; Basu, R.; Bhattacharya, S.; Singh, A.; Aswal, D. K.; Gupta, S. K.; Okram, G. S.; Ganesan, V.; Venkateshwarlu, D.; Surgers, C.; et al. Low Temperature Thermoelectric Properties of Cu Intercalated $TiSe_2$: A Charge Density Wave Material. *Appl. Phys. A: Mater. Sci. Process.* **2013**, *111*, 465−470.
(45) Snyder, G. J.; Toberer, E. S. Complex Thermoelectric Materials. *Nat. Mater.* **2008**, *7*, 105−114.

DOI: 10.1021/acs.chemmater.5b02572
Chem. Mater. XXXX, XXX, XXX−XXX